Metal-organic framework derived Ni/NiO micro-particles with subtle lattice distortions for high-performance electrocatalyst and supercapacitor

Yang Jiao, Weizhao Hong, Peiying Li, Lixin Wang, Gang Chen*

MIIT Key Laboratory of Critical Materials Technology for New Energy Conversion and Storage, School of Chemistry and Chemical Engineering, Harbin Institute of Technology, Harbin 150001, People's Republic of China

ABSTRACT

Herein, an effective and novel strategy has been designed to increase electrochemical reaction active sites in Ni/NiO nanoparticles prepared by optimizing the annealing temperature of nickel-based metal organic framework (Ni-MOF). Note that the incorporation of Ni^{3+} into the primitive lattice of Ni/NiO nanoparticles will cause a subtle atomic rearrangement, providing a large number of electrochemical reaction active sites. The density functional theory (DFT) simulation results also exhibit that the introduction of Ni^{3+} significantly lowers the gibbs free energy of atomic hydrogen absorption on the surface of Ni/NiO, benefiting H_2 gas evolution. On the basis of the above advantages, the as-synthesized Ni/NiO nanoparticles exhibit excellent performance for supercapacitors (SCs, the areal specific capacitance of $684.4\,m\,F\,cm^{-2}$ at $1\,mA\,cm^{-2}$) and Hydrogen evolution reaction (HER, ultralow overpotential of $41\,mV$ at $10\,mA\,cm^{-2}$). Significantly, the all-solid-state flexible asymmetric SCs based on Ni/NiO as anode and CNTs-COOH as cathode displays a high energy density of $61.3\,W\,h\,kg^{-1}$ at the power density of $900\,W\,kg^{-1}$. This work highlights the crucial role of the lattice distortion of materials for future applications in the sustainable energy storage and conversion.

1. Introduction

The increasing environment pollution and energy crisis have stimulated research on developing clean alternative and sustainable energy sources [1–4]. Hydrogen, a kind of clean energy, is regarded as a promising energy for future energy supply. Hydrogen evolution reaction (HER) in electrocatalytic water splitting is an important process for high-purity hydrogen production [5]. Now, the state-of-the-art catalyst to split water is platinum for the HER, but its limited resource reserves and expensive cost hinder the large scale application of this technology [6,7]. Meanwhile, supercapacitor, a novel and renewable energy storage device, has attracted wide attention due to their fast charge-discharge, long cycling life and high power densities [8]. However, the electrochemical active of electrode materials is a critical factor limiting the performance of supercapacitor [9,10]. Therefore, the search on effective and novel electrode materials to simultaneously meet the demands of highly-efficiency HER catalyst and supercapacitor is still a critical challenge for the development of the clean sustainable energy technology.

Recently, electrochemically active 3d transition metal oxides (TMOs) have been extensive researched as potential candidates in the fields of electrocatalysts and supercapacitors, due to their abundant earth resources and low cost [11]. Especially, Ni-based oxides with good electrical conductivity and high electrochemical activity have been as the key research object [12,13]. Nevertheless, the electrochemical property of the NiO shows suboptimal due to their exposure a limited number of the electrochemical reactive active sites. Focusing on this issue, several rational strategies were employed to further develop efficient electrode materials with abundant active sites and fast charge transfer ability. For example, Qiao et al. demonstrated that the introduction of oxygen vacancies into NiO lattices could produce more electrochemical active sites and improve the charge transfer ability of electrode materials [14]. Gong's group pointed out that the low-pressure thermal annealing process could be used to unfold and produce new active sites in Ni/NiO [15]. Nevertheless, the problem of poor electron transport during the electrochemical reaction process was still inevitable. It is still a considerable challenge to improve the electrochemical properties of Ni-based electrode materials by adjusting the exposed electrochemical reaction active sites at the atomic scale. Under the circumstances, the notion of introducing a subtle distortion into the nanostructures emerged in response to the abovementioned crisis. In general, the electronic configuration of NiO is $t_{2g}^{6}e_{g}^{2}$. Nevertheless, the abundant surface defects (nickel vacancies) introduced in NiO is obviously changing the e_g orbital occupancy of Ni^{2+} centers, producing

$t_{2g}^6 e_g^1$ electronic configuration (Ni^{3+}), and generating a local lopsided Coulomb force [16]. The exigent micromechanically derived impact will consequently cause subtle distortion in the arrangement of atomic, providing more exposed active sites of NiO for the electrochemical reaction [17,18]. Influenced by the above concept, on the basis of ensured stable electron transfer, constructing subtle distortion on the atomic scale is an effective and unique strategy to optimize the electrochemical active sites of NiO nanoparticles.

Heterostructured electrode materials have abundant interface active sites for charge transfer, and have attracted much attention in electrochemical filed [19,20], which stimulated us to distribute NiO to simultaneously control the morphology of NiO and enhance charge transfer rate and electrochemical performance. Metal-organic frameworks (MOFs) are a class of porous compounds and have been extensively used as ideal sacrificial templates due to the adjustability of their structures and morphologies [21–23]. They can be easily and selectively converted into the corresponding porous metal oxides, carbon materials or hybrid materials. Thereinto, Yamauchi's group have used a variety of MOFs as the sacrificial templates to derive various porous materials with adjustable unique morphology and outstanding functional performance improvement [24–28]. Herein, we reported a very simple approach to prepare electrode materials via calcining Ni-MOF and tune the surface defects of these electrode materials by controlling the calcination temperature. Nickel vacancies have been successfully introduced into the Ni/NiO nanostructures and generate a Jahn–Teller distortion mismatch between the Ni^{2+} ($t_{2g}^6 e_g^2$, There is no Jahn-Teller effect) and Ni^{3+} ($t_{2g}^6 e_g^1$, There is significant Jahn-Teller effect) coordination octahedral, which could give rise to the formation of subtle lattice distortion in Ni/NiO. The subtle lattice distortions in electrode materials are believed to promote faradaic reaction and HER activity [29]. The Ni/NiO calcined at 400 °C realizes an overpotential as low as 41 mV with a low Tafel slope of 59 mv dec^{-1} at the geometrical catalytic current density of 10 mA cm^{-2}. Meanwhile, the Ni/NiO-400 shows the highest areal specific capacitance. After assembling a flexible asymmetric supercapacitor with CNTs-COOH as cathode, and it achieves a high energy density of 61.3 W h kg^{-1} at a high power density of 900 W kg^{-1}.

2. Experimental section

All chemical reagents used were analytical grade and used without further purification. Nickel nitrate hexahydrate was purchased from Tianjin Zhiyuan Chemical reagent Co., Ltd. potassium hydroxide was purchased from Tianjin Kermel Chemical Reagent Co., Ltd. *p*-benzene-dicarboxylic acid (PTA) was purchased from Aladdin Industrial Corporation, N, N-dimethylformamide (DMF) was purchased from Shanghai Titan Scientific Co., Ltd.

2.1. Synthesis of Ni-MOFs

$Ni(NO_3)_2 \cdot 6H_2O$ and ligand (PTA) were dissolved in 10 mL and 5 mL DMF, respectively under vigorous stirring at room temperature for 20 min. Then, the DMF and $Ni(NO_3)_2 \cdot 6H_2O$ mixed solution was slowly added into PTA solution. Whereafter, citric acid (0.1 *g*) were dissolved in above solution. After fully stir, the as-prepared mixed solution was transferred into a 50 mL Teflon-lined stainless steel autoclave and reacted at 120 °C for 16 h. The precipitate was washed and centrifuged at 10 000 rpm with DMF and alcohol several times for 5 min. Finally, the products were fully dried with vacuum at 120 °C for 12 h.

2.2. Synthesis of Ni/NiO composites

Ni-MOF was annealed in air at 300, 350, 400, 450 °C with a rate of 5 °C min^{-1} for 2 h, respectively. The obtained products were named as Ni/NiO-300, Ni/NiO-350, Ni/NiO-400, Ni/NiO-450.

2.3. Characterization

Field emission scanning electron microscopy (SEM), transmission electron microscopy (TEM) energy and dispersive X-ray (EDX) mapping was recorded on FEI Quanta 200 F and TEM (Tecnai G^2 F30), respectively. X-ray diffraction (XRD) measurements were carried out by a Rigaku-D/MAX-2550 PC diffractometer (Cu-Kα radiation, λ = 0.1542 nm). Meanwhile, X-ray photoelectron spectroscopy (XPS) was collected by a Thermo Scientific ESCALAB 250Xi X-ray photoelectron spectrometer with a pass energy of 20 eV and an Al Kα excitation source (1486.6 eV). Thermogravimetric-differential scanning calorimetry (TG-DSC) was executed using Setsys Evolution instrumentation with a rate of 10 °C min^{-1} under ambient conditions. Raman spectra were carried out on a Renishaw via micro-Raman spectroscopy system.

2.4. Electrochemical measurements

Electrochemical measurements were conducted using electrochemical workstation (AUTOLAB PGSTAT302 N, Switzerland). For supercapacitor performance test, the working electrodes were prepared by mixing the active electrode material (80%), carbon black (10%) and polyvinylidene difluoride (PVDF 10%) in Nmethyl 2-pyrrolidinone for 12 h, after that the slurry was evenly coated onto carbon cloth current collectors with an area of 1 × 1 cm^2. The electrode was dried in a vacuum at 120 °C for 12 h and then pressed at 6 MPa. The mass loading for the electrode is about 1 mg. The electrocatalytic activity was tested in a standard three-electrode system, using N_2-saturated 1 M KOH solution (pH = 14), a Pt plate and a SCE as the electrolyte, counter and reference electrode, respectively. The polarization curves were measured at 5 mV s^{-1}, and all the measured potentials were referred to RHE using the following equation: E(RHE) = E(SCE) + 0.0592 × pH + 0.241. Stability test of the electrocatalysts were carried out by chronopotentiometry at 10 mA cm^{-2}. For supercapacitor test: the KOH (3 M), Pt plate and saturated calomel electrode were used as the electrolyte, counter electrode and reference electrode. Cyclic voltammetry (CV), galvanostatic charge–discharge (GCD) and electrochemical impedance spectroscopy (EIS) measurements were performed. The EIS data were collected with an AC voltage of 5 mV amplitude in the frequency range from 0.01 Hz to 100 kHz. The solid-state asymmetric surpercapacitore (ASC) was constructed by dissolving 6 g PVA into 30 mL H_2O and then mixed with 30 mL 3 M KOH solution. Finally, the two electrodes (Ni/NiO-400 positive electrode and CNT-COOH negative electrode) were immersed into PVA/KOH gel electrolyte for three min.

2.5. Computational details

The hydrogen adsorption energies are calculated using a 2 × 2 supercell (40 atoms) with 15 Å of vacuum to avoid interaction between layers. The first-principle DFT calculations were carried out using the Vienna Ab-initio Simulation Package code (VASP) [30–32]. The Generalized Gradient Approximation (GGA) in the parametrization by Perdew, Burk and Ernzerhof combined with the projector augmented wave (PAW) method was used [33]. A Monkhorst-Pack-centered 5 × 5 × 1 *k*-point mesh was used. Three layers were fixed and two layers were unrestricted during structural optimization. The relaxation proceeded until the forces acting on all the atoms became less than 0.02 eV/Å. Spinpolarization was taken into account in all calculations. The free energies of the intermediates were obtained by $\Delta G(H^*) = \Delta E(H^*) + \Delta ZPE - T\Delta S$, where $\Delta E(H^*)$ is the binding energy of H species, ΔZPE and ΔS are the zero point energy change and entropy change of adsorption H, respectively.

According to the Eq. (1) as follow, the areal specific capacitance of the electrode can be calculated from the discharge curves:

$$C = \frac{I \times \Delta t}{S \times \Delta V} \qquad (1)$$

where C is the areal specific capacitance (mF cm^{-2}), I is the discharge current (mA) and Δt is the discharge time (s), S (cm^2) is the areal of the active electrodes, ΔV is the potential window of electrode, respectively.

In the ASC systems, the charge balance between the positive and negative needs to follow the relationship $q^+ = q^-$, the optimal mass ratio between the two electrodes can be obtained according to the following Eq. (2):

$$\frac{m^+}{m^-} = \frac{C^- \times \Delta V^-}{C^+ \times \Delta V^+} \qquad (2)$$

where m^+, C^+ and ΔV^+ are the mass, areal specific capacitance and potential window of the positive electrode respectively, m^-, C^- and ΔV^- are the mass, areal specific capacitance and potential window of the negative electrode, respectively.

The power density (P) and energy density (E) of the energy storage devices were calculated based on the Eq. (3) and Eq. (4) as follow:

$$E = \frac{1}{2}C\Delta V^2 \qquad (3)$$

$$P = \frac{E}{\Delta t} \qquad (4)$$

where C is the specific capacitance of the asymmetric supercapacitors calculated according to the discharge curves based on the total weight of the electrochemical active materials in two electrodes, P (W kg^{-1}), E (W h kg^{-1}), Δt (s) and ΔV (V) represent the power density, energy density, discharge time and voltage window, respectively.

3. Results and discussion

3.1. Structural and morphological analysis

The Ni/NiO-X (X = 300, 350, 400 or 450 °C) electrode materials are prepared by thermolysis of the Ni-MOF at different temperatures in nitrogen atmospheres for 2 h. The thermal gravimetric analysis (TGA, Fig. S1a) result shows Ni-MOF is completely decomposed at above 340 °C. X-ray diffraction (XRD, Fig. S1b) measurements further confirmed that the coexistence of metallic Ni (PDF: 04-0850) and NiO (PDF: 47–1049) by calcination at or more than 350 °C. The broad peaks of as-obtained Ni/NiO in the XRD may be attributed to nano-sized particles or low crystallinity.

Scanning electron microscopy (SEM, Fig. 1a–c) and transmission electron microscopy (TEM, Fig. 1g) images of as-synthesized microspheres (Ni/NiO-400) showed the rough surface morphology composing of closely packed particles with a size of 30–40 nm. Meanwhile, the effects of calcination temperature on the morphologies of as-prepared materials were researched for comparative study, as shown in Fig. S2, S3. The number of nanoparticles on the surface of microspheres increases with the increase of the calcination temperature. It has been theoretically proved that the rough surface environment of electrode materials can offer better electrochemical performance than that of smooth surface, due to the increased chemical reaction active site on their surface [34,35]. Further high-resolution transmission electron microscopy (HRTEM) analysis (Fig. 1d–f) indicated that the lattice fringes with spacing of 0.147, 0.12 and 0.176 nm are indexed to the (220) and (222) faces of NiO, and (200) face of Ni, respectively. The fast Fourier transform (FFT) pattern (inset of Fig. 1d) further proved the existence of (200), (220) and (331) lattice planes. Interesting, we clearly observed the tiny lattice distortions in some parts of the HRTEM image, the twisted (red-marked) and regular (yellow-marked) atomic arrangement on the surface of electrode material are simultaneously observed, as shown in Fig. 1f. This subtle lattice distortion may be conductive to the formation of the high conductivity and the additional electrochemical reaction active sites [36,37]. In addition, the formation of micro-spheres can be further confirmed by a high-angle annular dark-field scanning transmission electron microscopy (HAADF–STEM) image (Fig. 1g), and the corresponding energy-dispersive X-ray (EDX) mappings showed that the Ni, C and O atoms were distributed equably over all samples (Fig. 1h–k). Thereinto, carbon comes from the decomposition of organic ligands.

3.2. Electrocatalytic activity

The three-electrode system was used to test the HER performance of the Ni/NiO-X electrods in 1 M KOH electrolyte, as shown in Fig. 2. The carbon cloth showed an overpotential of 477 mV at a current density of 10 mA cm^{-2}, indicating the poor HER activities. It can be noted that the Ni/NiO-400 only needs 41 mV overpotential to obtain a current density of 10 mA cm^{-2} and the overpotential of 170 mV at 40 mA cm^{-2} current density. In comparison, Ni/NiO-300, Ni/NiO-350 and Ni/NiO-450 showed a high overpotential of 339, 64 and 114 mV, respectively, at a current density of 10 mA cm^{-2} (Fig. 2a). As we know, the Ni/NiO-400 is
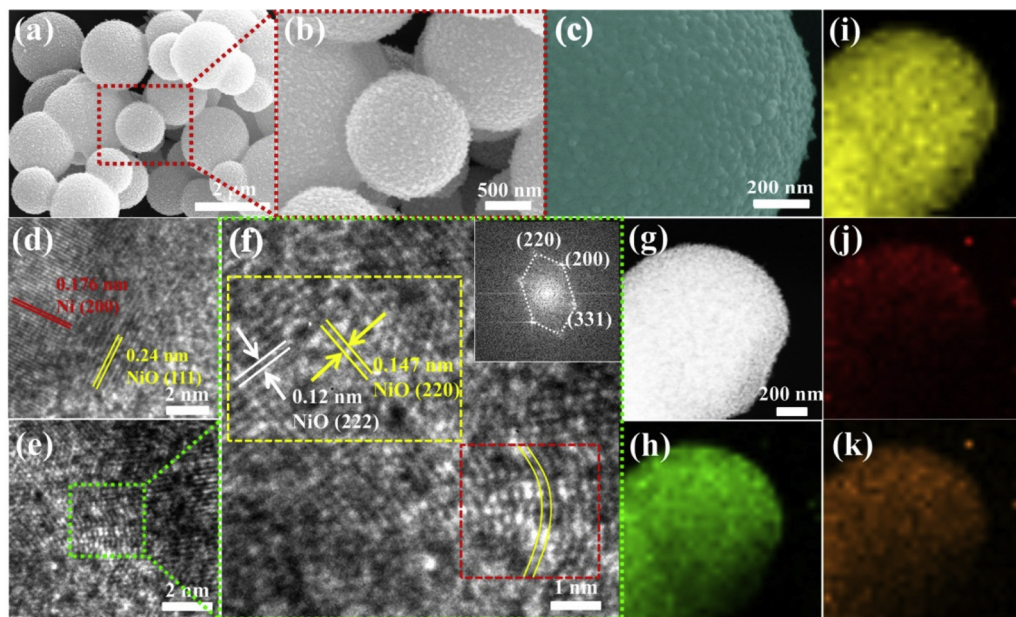

Fig. 1. (a–c) SEM images of Ni/NiO-400, (d) HRTEM image and corresponding FFT patterns (insets), (e) The TEM image, The magnified image in (f) clearly reveals the subtle distortion regions by red dotted line, (g) HAADF-STEM image. (h–k) EDX maps for combined image (h), Ni (i), C (j) and O (k) (For interpretation of the references to colour in this figure legend, the reader is referred to the web version of this article).
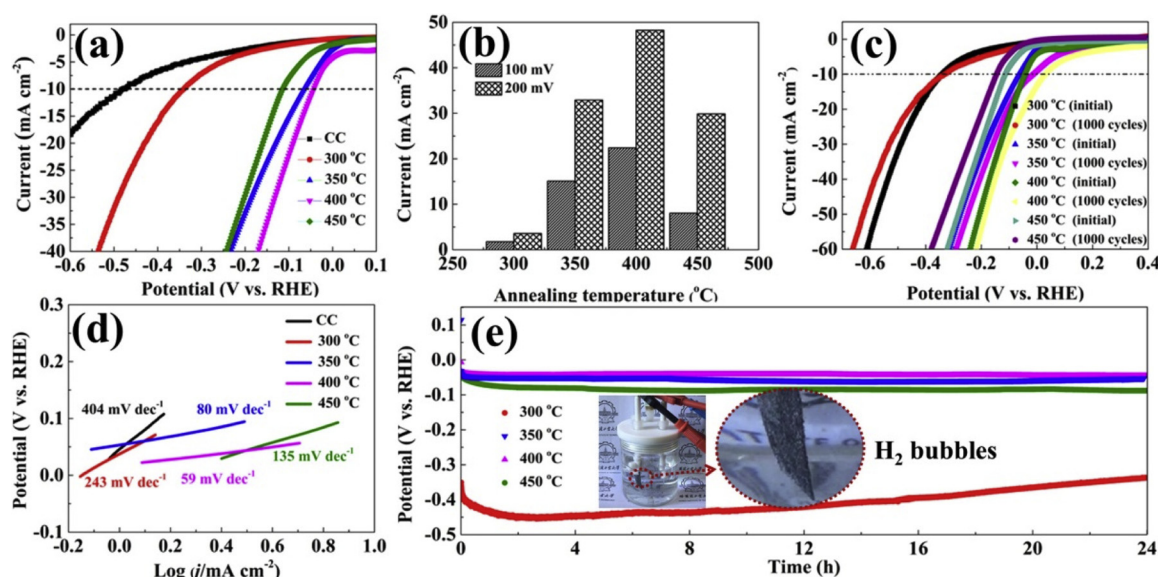
Fig. 2. (a) HER polarization curves for Ni/NiO samples prepared at different temperatures on Carbon cloth electrode compared to those of a blank Carbon cloth electrode, (b) Current densities at overpotentials of 100 mV and 200 mV, (c) Durability measurements, (d) The Tafel plots, (e) Cycling stability of electrodes measured by chronopotentiometry at a current density of 10 mA cm^{-2}.

one of the most efficient nickel-based HER electrocatalyst reported by far (see Table S1, Supporting Information). Fig. 2b further indicated that the Ni/NiO-400 has the highest current density than others Ni/NiO-X samples under the same overpotential condition. These results indicating that the Ni/NiO-400 exhibited the highest electrocatalytic activity. Furthermore, the Ni/NiO-X electrodes exhibited a stable cycle performance by 1000 cycle linear sweep voltammetry (LSV) measurements (Fig. 2c) and during a continuous chronoptentiometry test at a current density of 10 mA cm^{-2} for 24 h (Fig. S3). The cycle performance of Ni/NiO-300 showed an outstanding improvement, which may be attributed to that the weak Ni-ligand coordination bond was broken during electrochemical process and was replaced by stronger Ni−OH bond to form Ni(OH)$_2$ [38,39]. The Tafel slopes based on LSV curves revealed the HER kinetic process of Ni/NiO-X electrodes, as shown in Fig. 2d. The expectedly Tafel slope of ∼ 59 mV dec^{-1} was obtained for Ni/NiO-400, indicating that the HER is dominated by a Volmer-Heyrovsky mechanism [40,41]. The bubbles of H$_2$ can be clearly discovered on the surface of Ni/NiO-400 electrode, as shown in the inset of Fig. 2e and Movie S1.

Meanwhile, the values of ∼404 mV dec^{-1}, 243 mV dec^{-1}, 80 mV dec^{-1} and 135 mV dec^{-1} were obtained for carbon cloth, Ni/NiO-300, Ni/NiO-350 and Ni/NiO-450, respectively. To find the control factors of the electrochemical performance of Ni/NiO-X, we conducted Raman analysis and X-ray photoelectron spectroscopy (XPS) analysis.

According to previous literature reports, the carbon shells of graphitic carbon too thick may significantly reduce the catalytic activity. However, the introduction a thin layer of graphitized carbon into metallic oxides may have an energetic effect on the electrochemical performance [42–44]. Raman analysis firstly eliminated the effect of graphitized carbon for Ni/NiO-X on the electrochemical activity (Fig. S4). Fig. S4 showed that the graphitized carbon content decreased gradually with the increase of annealing temperature, and the corresponding the activity of HER increased and reached the maximum when the electrode prepared at 400 ℃. Further increase the annealing temperature will lead to a slightly low electrochemical activity. We hypothesize that there may be other reasons to offset the contribution of the graphitized carbon to the electrochemical activity, resulting in a high HER activity for Ni/NiO-400. In order to further explore the reason of the excellent electrochemical performance of Ni/NiO-400, the X-ray photoelectron spectroscopy (XPS) analysis was employed (Fig. 3). Fig. 3a revealed

that the existence of Ni, O and C in samples, consistent with the EDX mapping results (Fig. 1i). The Ni$_{2p}$ spectra of samples are shown in Fig. 4b–e, the content of Ni° increases with the increase of calcination temperature, which is not consistent with the trend of electrochemical performance (Fig. 3f). Therefore, we have eliminated the effect of Ni°. Meanwhile, the relative intensity of Ni^{3+}/Ni^{2+} in Ni/NiO-400 is higher than that of others samples, which is in good agreement with the trend of electrochemical performance on samples. Therefore, we deduce that this unique electronic structure of Ni/NiO-400 with a lot of Ni^{3+} defects was expected to improve the electrochemical performance of electrode material. The Ni^{3+} of in samples is from V$_{Ni}$ created during the calcination process. In order to obtain charge balance near the V$_{Ni}$, Ni^{2+} is oxidized to Ni^{3+} [45]. A large number of Ni^{3+} defects (Fig. 3f) may be led to an innovative subtle lattice distortion on the surface of materials. The reasons are as follow: first, the localized Coulomb interaction around the Ni atoms arising from the introduction of the incoordinate electron spins [17]. Second, the Jahn–Teller distortion mismatch between the Ni^{2+} (perfect octahedral structure) and Ni^{3+} (distorted octahedral structure) coordination octahedral [18], as shown in Fig. 4. (Ni^{2+}, t$_{2g}$^{6}e$_g$^{2}, eg orbitals are equally occupied, no Jahn-Teller effect; Ni^{3+}, t$_{2g}$^{6}e$_g$^{1}, eg orbitals are unequally occupied, there is significant Jahn-Teller effect,). The electrochemical active specific area (ECSA) of electrode materials can be used to further know the reason for obvious difference in HER catalytic performance. The extracting the double-layer capacitance (C$_{dl}$) is expected to be linearly proportional to the actual effective ECSA in the electrode materials. As shown in Fig. S5, the C$_{dl}$ of the Ni/NiO-400 sample is slightly higher than the other samples. This relatively large C$_{dl}$ numbers clearly indicate that the Ni/NiO-400 has more exposed electrochemical active sites. The results further prove that the strategy of introducing abundant Ni^{3+} into Ni/NiO lattice can produce additional electrochemical atomic active sites and improve HER performance.

The hydrogen binding energy (HBE) has been proved as a useful approach to further insights into the HER activity. Fig. 5 shows the density functional theory (DFT) calculations of NiO without and in presence of Ni^{3+} (V$_{Ni}$) in the NiO, and corresponding models are shown in Fig. 5a–c. The electrochemical processes of HER can be showed in a three-state diagram, consisting of an initial H$^+$ state, an intermediate H* state and 1/2 H$_2$ (Fig. 5d). An ideal electrocatalyst of the HER should have a moderate free energy for H adsorption (ΔG$_{H*}$) to facilitate the
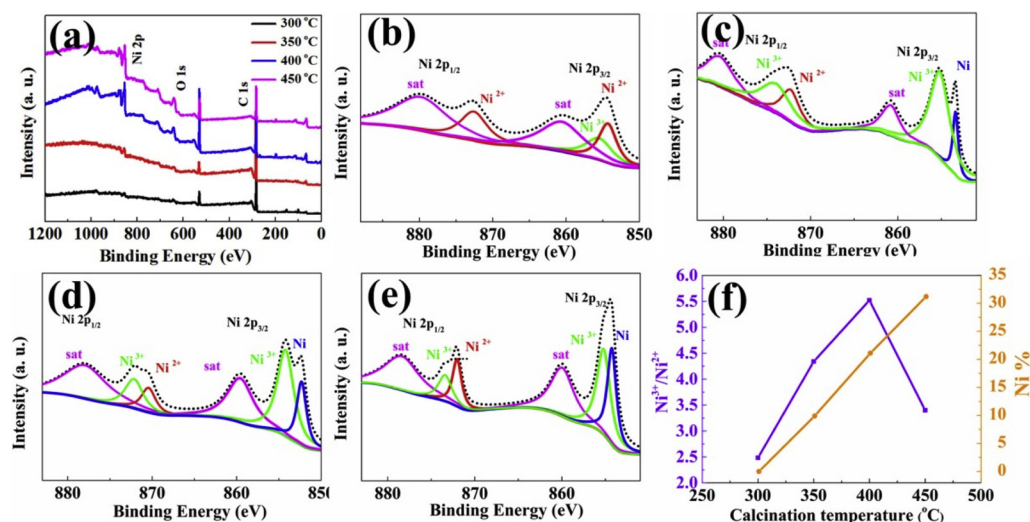
Fig. 3. (a) XPS spectra, Ni_{2p} XPS spectrum of Ni/NiO prepared at different annealing tempertures (b) 300 °C, (c) 350 °C, (d) 400 °C, (e) 450 °C, and (f) the surface composition obtained from XPS.
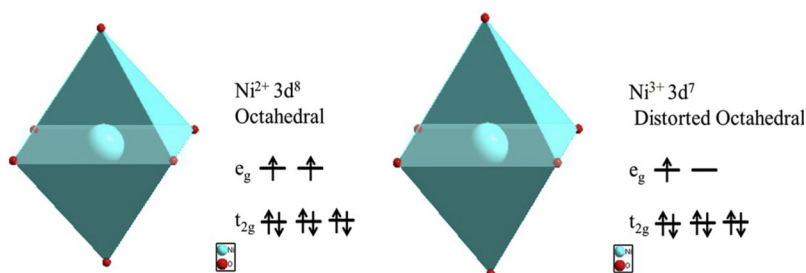

Fig. 4. Schematic electronic configuration of the Ni cations in NiO.

adsorption and desorption steps [46]. The ΔG_{H*} value of the bulk NiO was calculated to be 0.554 eV, indicating a weaken H^* adsorption on NiO, which leads to a low HER activity [47]. Meanwhile, the ΔG_{H*} value of V_{Ni} doping in NiO shifted to 0.293 eV, manifesting a relatively close to the ideal H^* adsorption value of 0 eV and resulting in a high HER activity [48]. In our DFT calculations, the existence of Ni^{3+} significantly strengthen the adsorption of H^* on NiO, which well explained the great HER electrocatalytic activity of Ni/NiO-400. The reason for the increased performance is explained schematically in Fig. 6, where the six nearest O atoms are getting closer to V_{Ni}, significantly increasing the average distance of neighboring Ni^{2+} and O atoms. Meanwhile, the electron cloud density of near the Ni^{2+} increases, which leading to a strong H^* adsorption.

3.3. Supercapacitor performance analysis

Except for electrocatalytic performances, supercapacitor performances of the Ni/NiO-X were also researched in a three-electrode system. Fig. 7a shows the cyclic voltammetry curves (CV) of Ni/NiO-X measured at a scan rate of 5 mV s^{-1}. A couple of redox peaks can be found from the CV curves, which can be attribute to the Faradic reaction between Ni^{2+}/Ni^{3+} with OH^-. Moreover, the area of the CV curve is an indicator for the specific capacity, indicating that Ni/NiO-400 has a much better supercapacitor performance than that of other electrodes. The CV curves of the Ni/NiO-X electrodes at different scan rates (Fig. S6 and Fig. 7b) show the peak positions only shift a little, manifesting good electrical reversibility [49,50]. Moreover, Fig. 7c demonstrates the galvanostatic charge–discharge (GCD) curves of different electrode materials at current density of 1 mA cm^{-1} with the potential window from 0 V to 0.45 V (vs. SCE). The discharge time of Ni/NiO-400 is
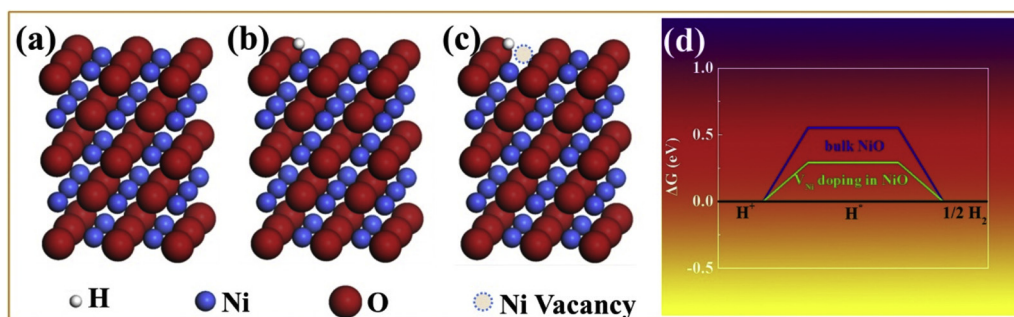
Fig. 5. (a) Models of pristine NiO, (b) theoretical simulation the adsorption of H atom on surface of NiO without Ni vacancy and (c) with Ni vacancy, respectively, (d) Gibbs free energy profiles of HER on different electrocatalysts.
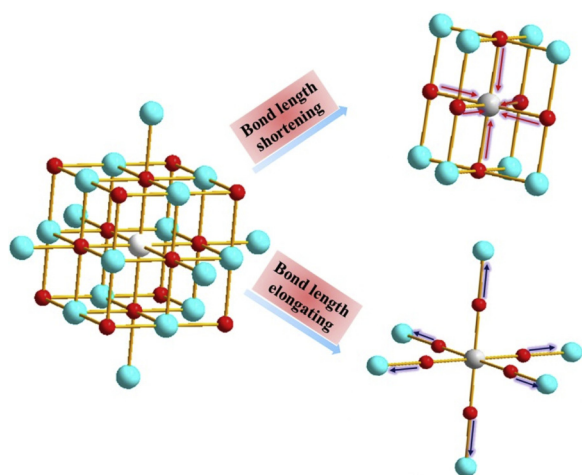
Fig. 6. schematic view of the Ni and O atoms relaxation around V_{Ni} in Ni/NiO.

longer than that of other electrodes, indicating a much larger specific capacity and matching well with the CV results. (the GCD curves of the Ni/NiO-300, Ni/NiO-350, Ni/NiO-400 and Ni/NiO-450 collected at various current densities can be found in Fig. 7d and Fig. S5). Fig. 7e shows the specific capacities as a function of current density calculated based on the GCD curves. Note that at a small current density of 1 mA cm^{-2}, Ni/NiO-400 shows high area specific capacity of 684.4 m F cm^{-2}. The area specific capacity of 133.3 F cm^{-2} can be obtained even at a high current density of 30 mA cm^{-2}, indicating a remarkable rate capability of Ni/NiO-400. Electrochemical impedance spectroscopy (EIS) was employed at a frequency range from 100 kHz to 0.01 Hz to better understand the conductivity of different samples, as shown in Fig. 7f. In the high frequency ranges, the semicircle radiuses of the electrodes are similar except for the intercept of the real axis, which relates to the equivalent series resistance (ESR) [51]. This represents the low solution resistance and intrinsic resistance of Ni/NiO-400. The cycling stability of Ni/NiO-400 was researched by GCD test. Based on the discussion above, the excellent electrochemical performance of the Ni/NiO-400 can be attributed to the following aspects. First, the rough surface of active materials will consequentially increase the specific surface areas of electrode materials and promote the rapid transfer of electrons [52].

Second, the interface of heterostructures will lead to abundant electrochemical reaction active sites, facilitating the transport and diffusion of electrolyte ions [53]. Third, the unique and abundant lattice distortion structures of Ni/NiO-400 can provide sufficient reaction active sites. Fourth, abundant Ni^{3+} sites exist in the form of NiOOH, which has a significant influence on the electrical conductivity of the material and promotes the efficiency of the charge transfer.

To evaluate the feasibility of the as-obtained Ni/NiO-400 for practical application, an all-solid-state flexible asymmetric supercapacitor (ASC) was assembled by using the Ni/NiO-400 as the anode, the carboxylic acid functionalized carbon nanotubes (CNTs-COOH) as the cathode and PVA/KOH as the flexible electrolyte, as illustrated in Fig. 8a. The SEM image and electrochemical performances of CNTs-COOH electrode are showed in Fig. S7 and Fig. S8, respectively. Meanwhile, the storage charge (Q+ = Q-) between the two electrodes has also been balanced. The assembled SCs could utilize the potential range of Ni/NiO and CNTs-COOH to attain a high voltage window (According to the CV and GCD curves, Fig. 8b and c). CV curves of ASC at different voltage ranges (Fig. 8d) and various scan rates (Fig. 8e) show that this device can successfully

work at 1.8 V with excellent capacitive behavior. Moreover, the overall specific capacitance of the Ni/NiO//CNTs-COOH ASC device is come from the combined contribution of Faradaic pseudocapacitance and EDLC-type capacitance, simultaneously. The GCD curves are shown in Fig. 8f, based on the corresponding discharge time, the areal specific capacitance is calculated to be 136.4, 119, 78, 70 and 62.6 F g^{-1} at the current density of 2, 4, 10, 16 and 20 mA cm^{-2}, respectively (Fig. S9). Fig. 8g presents the corresponding Ragone plot of the ASC, this device delivered a high energy density of 61.3 W h kg^{-1} at the power density of 900 W kg^{-1}, which maintained at 28.2 W h kg^{-1} at a high power density of 9064 W kg^{-1}. Compared to the other supercapacitor electrode materials shown in Table S4, the electrochemical performance of Ni/NiO// CNTs-COOH is found superior to those of Ni-based asymmetric supercapacitors. The cycling performance of the Ni/NiO//CNTs-COOH asymmetric supercapacitors was evaluated at a high current density of 10 A g^{-1} (Fig. 8h). It can be clearly observed that the Ni/NiO//CNTs-COOH asymmetric supercapacitor displays excellent cycling stability with about 92.8% of the initial specific capacitance even after 10,000 cycles. In addition, in the supporting information, we take the SEM images of the Ni/NiO electrode before (Fig. 1a) and after 10,000 cycles (Fig. S10). Amazingly, it shows that the morphologies of the Ni-NiO
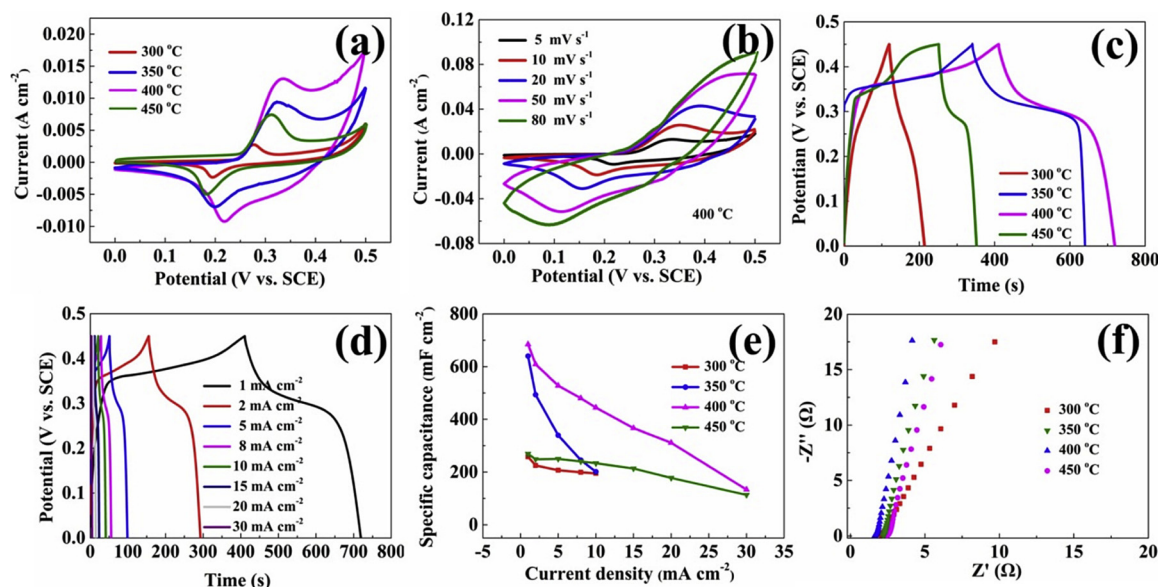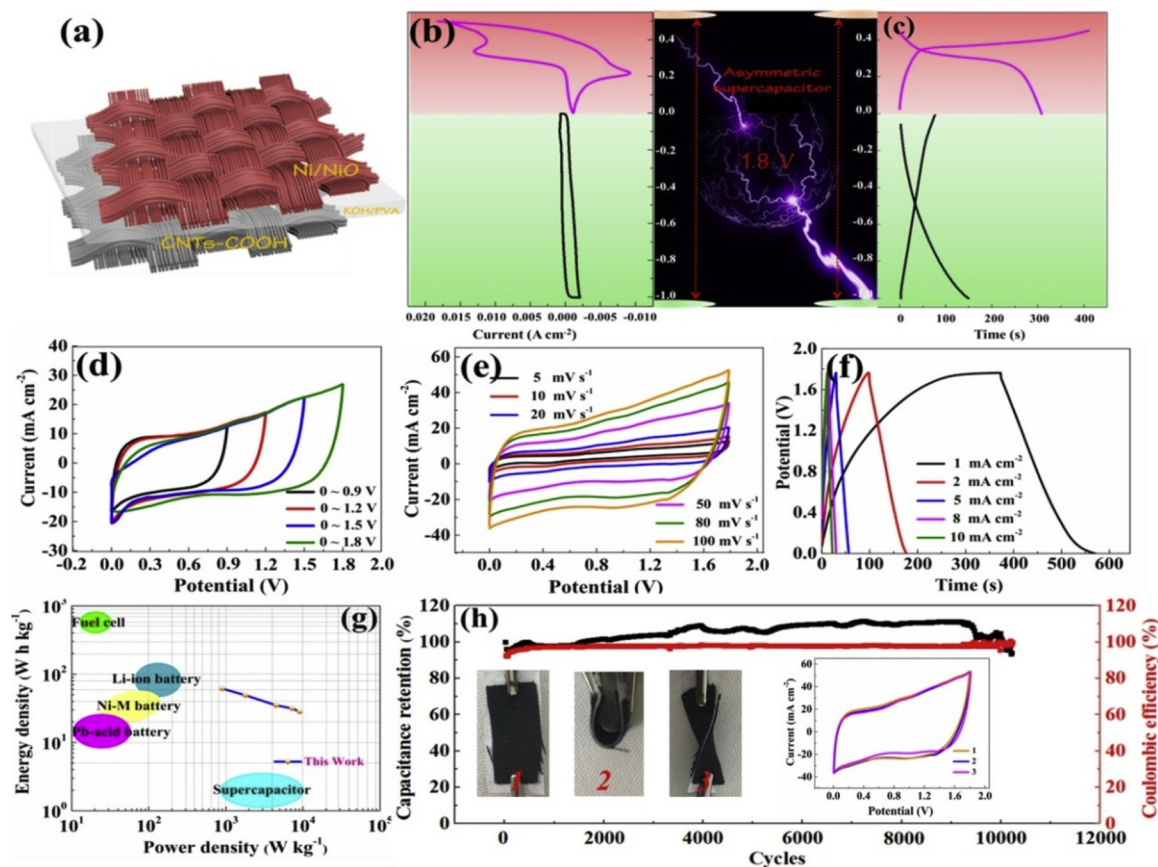

Fig. 7. (a) CV curves comparison, (b) CV curves of Ni/NiO-400 at different scan rates, (c) GCD curves comparison, (d) GCD curves of Ni/NiO-400 at different current densities, (e) A summary of areal specific capacitance versus current density comparison and (f) Ragone plots comparison.

Fig. 8. (a) Schematic structure of the solid-state ASCs, (b) CV curves of the Ni/NiO and CNTs-COOH electrodes at a scan rate of 5 mV s^{-1}, (c) GCD curves of the Ni/NiO and CNTs-COOH electrodes at a current density of 1 mA cm^{-2}, (d) CV curves at different potentials. e) CV curves of the ASC at different scan rates, (f) GCD curves of the ASC at different current densities, (g) The Ragone plots, (h) Cycling performance, the inset is ASC undergo (1) 0° (2) 80° bending and (3) twisting, (4) CV curves of ASC collected at 20 mV s^{-1} under different bending conditions.

composites haven't changed obviously and only a few of the Ni-NiO nanospheres aggregated compared with that of the as-prepared Ni/NiO nanospheres after cycles. The superior electrochemical properties of Ni/NiO composites indicate that the specific structure can relax the collapse of the structure cause by the volume expansion during cycling. Furthermore, the CV curves have almost no obvious change, even when the ASC on carbon cloth was bended and twisted during the electrochemical test (inset in Fig. 8h), which demonstrates this device has a remarkable mechanical flexibility and practical application value.

4. Conclusion

In summary, we have successfully designed and fabricated the Ni/NiO nanoparticle with subtle lattice distortions by using Ni-MOF as precursors and templates. Such heterostructures would undisputedly lead to the increase of the specific surface area and interface sites of electrode materials and facilitate the fast transportation of electrolyte ions and electrons, improving the electrochemical performance. Superior flexible supercapacitive property and electrocatalytic hydrogen evolution reaction property of the Ni/NiO electrode mainly is the introduction of Ni^{3+} in Ni/NiO to cause distorted atomic arrangement, thus exposing more active sites. Moreover, Density functional theory (DFT) calculations indicate that the existence of Ni^{3+} significantly lowers free energy for atomic hydrogen absorption on Ni/NiO, ensures fast hydrogen evolution kinetics. This work provides a new opportunity to design various nano-structures at the atomic level. Furthermore, these nano-materials have abundant electrochemical reaction active sites, which can be used in high-efficient flexible electrochemical energy conversion and storage fields.

Appendix A. Supplementary data

Supplementary material related to this article can be found, in the online version, at doi:https://doi.org/10.1016/j.apcatb.2018.11.035.

References

[1] M. Salanne, B. Rotenberg, K. Naoi, K. Kaneko, P.L. Taberna, C.P. Grey, B. Dunn, P. Simon, Nat. Energy 1 (2016) 1–10.
[2] Y. Jiao, G. Chen, D. Chen, J. Pei, Y. Hu, J. Mater. Chem. A 5 (2017) 23744–23752.
[3] Y. Liu, H. Zhang, J. Ke, J. Zhang, W. Tian, X. Xu, X. Duan, S. Wang, Appl. Catal. B: Environ. 228 (2018) 64–74.
[4] Y. Qin, X.D. Wang, Z.L. Wang, Nature 451 (2008) 809–813.
[5] S. Emin, C. Altinkaya, A. Semerci, H. Okuyucu, A. Yildiz, P. Stefanov, Appl. Catal. B: Environ. 236 (2018) 147–153.
[6] L. Zhang, J. Lu, S. Yin, L. Luo, S. Jing, A. Brouzgou, J. Chen, P.K. Shen, P. Tsiakaras, Appl. Catal. B: Environ. 230 (2018) 58–64.
[7] S. Jing, L. Zhang, L. Luo, J. Lu, S. Yin, P.K. Shen, P. Tsiakaras, Appl. Catal. B: Environ. 224 (2018) 533–540.
[8] Y. Jiao, J. Pei, C. Yan, D. Chen, Y. Hu, G. Chen, J. Mater. Chem. A 4 (2016) 13344–13351.
[9] W.H. Li, K. Ding, H. Tian, M.S. Yao, B. Nath, W.H. Deng, Y. Wang, G. Xu, Adv. Funct. Mater. 27 (2017) 1702067.
[10] Y. Jiao, Y. Liu, B.S. Yin, S.W. Zhang, F.Y. Qu, X. Wu, Nano Energy 10 (2014) 90–98.
[11] G. Cheng, T. Kou, J. Zhang, C. Si, H. Gao, Z. Zhang, Nano Energy 38 (2017) 155–166.
[12] Z. Zhou, F. Chen, T.R. Kuang, L. Chang, J. Yang, P. Fan, M.Q. Zhang, Electrochim. Acta 27 (2018) 288–297.
[13] M. Yu, W. Wang, C. Li, T. Zhai, X. Lu, Y. Tong, NPG Asia Mater. 6 (2014) 129.

[14] T. Zhang, M.Y. Wu, D.Y. Yan, J. Mao, H. Liu, W.B. Hu, X.W. Du, T. Ling, S.Z. Qiao, Nano Energy 43 (2018) 103–109.

[15] M. Gong, W. Zhou, M.C. Tsai, J. Zhou, M. Guan, M.C. Lin, B. Zhang, Y. Hu, D.Y. Wang, J. Yang, S.J. Pennycook, B.J. Hwang, H. Dai, Nat. Commun. 5 (2014) 4695.

[16] Y. Zhao, X. Jia, G. Chen, L. Shang, G.I.N. Waterhouse, L.Z. Wu, C.H. Tung, D.O. Hare, T. Zhang, J. Am. Chem. Soc. 138 (2016) 6517–6524.

[17] C. Xia, H. Liang, J. Zhu, U. Schwingenschlögl, H.N. Alshareef, Adv. Energy Mater. 7 (2017) 1602089.

[18] Y. Liu, X. Hua, C. Xiao, T. Zhou, P. Huang, Z. Guo, B. Pan, Y. Xie, J. Am. Chem. Soc. 138 (2016) 5087–5092.

[19] A. Pendashteh, J. Palma, M. Anderson, R. Marcilla, Appl. Catal. B: Environ. 201 (2017) 241–252.

[20] M. Gong, W. Zhou, M.C. Tsai, J. Zhou, M. Guan, M.C. Lin, B. Zhang, Y. Hu, D.Y. Wang, J. Yang, S.J. Pennycook, B.J. Hwang, Nat. Commun. 5 (2014) 4695.

[21] C. Guan, X. Liu, W. Ren, X. Li, C. Cheng, J. Wang, Adv. Energy Mater. 7 (2017) 1602391.

[22] R.R. Salunkhe, J. Tang, Y. Kamachi, T. Nakato, J.H. Kim, Y. Yamauchi, ACS Nano 9 (2015) 6288–6296.

[23] R. Bendi, V. Kumar, V. Bhavanasi, K. Parida, P.S. Lee, Adv. Energy Mater. 6 (2015) 1501833.

[24] R.R. Salunkhe, Y.H. Lee, K.H. Chang, J.M. Li, P. Simon, J. Tang, N.L. Torad, C.C. Hu, Chem. Eur. J. 20 (2014) 13838–13852.

[25] R.R. Salunkhe, J. Tang, N. Kobayashi, J. Kim, Y. Ide, S. Tominaka, J.H. Kim, Y. Yamauchi, Chem. Sci. 7 (2016) 5704–5713.

[26] J. Tang, Y. Yamauchi, Nat. Chem. 8 (2016) 638–639.

[27] R.R. Salunkhe, C. Young, J. Tang, T. Takei, Y. Ide, N. Kobayashi, Y. Yamauchi, Chem. Commun. 52 (2016) 4764–4767.

[28] R.R. Salunkhe, Y.V. Kaneti, Y. Yamauchi, ACS Nano 11 (2017) 5293–5308.

[29] I.L. Chen, Y.C. Wei, K.T. Lu, T.Y. Chen, C.C. Hu, J.M. Chen, Nanoscale 7 (2015) 15450–15461.

[30] T. Bučko, J. Hafner, S. Lebègue, J.G. Ángyán, J. Phys. Chem. A 114 (2010) 11814–11824.

[31] X. Meng, G. Zhang, N. Li, Chem. Eng. J. 314 (2017) 249–256.

[32] E.S. Iason, V. Tripkovic, M.E. Bjo¨rketun, S. Gudmundsdo´ttir, G. Karlberg, J. Rossmeisl, T. Bligaard, H. Jo´nsson, J.K. Nørskov, J. Phys. Chem. C 114 (2010) 18182–18197.

[33] P.E. Blo¨chl, Phys. Rev. B (1994) 17953.

[34] W. He, C. Wang, H. Li, X. Deng, X. Xu, T. Zhai, Adv. Energy Mater. (2017) 1700983.

[35] X. Xie, Z. Ao, D. Su, J. Zhang, G. Wang, Adv. Funct. Mater. 25 (2015) 1393–1403.

[36] J. Deng, H. Li, J. Xiao, Y. Tu, D. Deng, H. Yang, H. Tian, J. Li, P. Ren, X. Bao, Energy Environ. Sci. 8 (2015) 1594–1601.

[37] D.Y. Wang, M. Gong, H.L. Chou, C.J. Pan, H.A. Chen, Y.P. Wu, M.C. Lin, M.Y. Guan, J. Yang, C.W. Chen, Y.L. Wang, B.J. Hwang, C.C. Chen, H.J. Dai, J. Am. Chem. Soc. 137 (2015) 1587–1592.

[38] C. Qu, Y. Jiao, B. Zhao, D.C. Chen, R.Q. Zou, K.S. Walton, M.L. Liu, Nano Energy 26 (2016) 66–73.

[39] Y. Jiao, J. Pei, D. Chen, C. Yan, Y. Hu, Q. Zhang, G. Chen, J. Mater. Chem. A 5 (2017) 1094–1102.

[40] J. Deng, P.J. Ren, D.H. Deng, L. Yu, F. Yang, X.H. Bao, Energy Environ. Sci. 7 (2014) 1919–1923.

[41] D.W. Zhang, J. Li, J.X. Lou, Nanotechnology 29 (2018) 245402.

[42] D.H. Deng, L. Yu, X.Q. Chen, G.X. Wang, L. Jin, X.L. Pan, J. Deng, G.Q. Sun, X.H. Bao, Angew. Chem. Int. Ed. 52 (2013) 371–375.

[43] X.J. Zheng, J. Deng, N. Wang, D.H. Deng, W.H. Zhang, X.H. Bao, C. Li, Angew. Chem. Int. Ed. 53 (2014) 7023–7027.

[44] Y.J. Gao, G. Hu, J. Zhong, Z.J. Shi, Y.S. Zhu, D.S. Su, J.G. Wang, X.H. Bao, D. Ma, Angew. Chem. Int. Ed. 52 (2013) 2109–2113.

[45] B. Sasi, K.G. Gopchandran, Nanotechnology 18 (2007) 115613.

[46] Y. Luo, X. Li, X.K. Cai, ACS Nano 12 (2018) 4565–4573.

[47] Y.J. Ko, J.M. Cho, I. Kim, J.K. Park, Y.J. Baik, H.J. Choi, W.S. Lee, Appl. Catal. B: Environ. 203 (2017) 684–691.

[48] J. Deng, P. Ren, D. Deng, X. Bao, Angew. Chem. Int. Ed. 54 (2015) 2100–2104.

[49] H. Chen, L. Hu, M. Chen, Y. Yan, L. Wu, Adv. Funct. Mater. 7 (2014) 934–942.

[50] C. Couly, M. Alhabeb, K.L. Van Aken, N. Kurra, L. Gomes, A.M. Navarro Suárez, B. Anasori, H.N. Alshareef, Y. Gogotsi, Adv. Electron. Mater. 4 (2018) 1700339.

[51] R. Rajagopal, K.S. Ryu, Appl. Catal. B: Environ. 236 (2018) 125–139.

[52] W. Chen, C. Xia, H.N. Alshareef, ACS Nano 8 (2014) 9531–9541.

[53] L. Mei, T. Yang, C. Xu, M. Zhang, L. Chen, Q. Li, T. Wang, Nano Energy 3 (2014) 36–45.